Check for updates

ADVANCED FUNCTIONAL MATERIALS
www.afm-journal.de

Phase Junction Induction Through Atomic Ratio Tuning of Molybdenum Carbides for Enhanced Stepwise Iodine Conversion

*Song Chen, Jizhen Ma, Qianwu Chen, Wenshuo Shang, Jinshuai Liu, Junhao Shang, Yanxu Wang, and Jintao Zhang**

Iodine redox conversion often suffers from polyiodide formation and deactivation due to the shuttle effect. To address these challenges, the atomic ratio of molybdenum carbide (Mo_xC) nanoclusters are modulated, uniformly dispersed within nitrogen-doped carbon, to induce distinct phase-junctions through a flash Joule heating method. This strategy not only physically traps iodine within porous carbon but also strengthens chemisorption by forming Mo_xC phase junctions, facilitating efficient iodine conversion. The resulting built-in electric field accelerates charge migration, promoting the reduction of polyiodides to iodide ions and enhancing overall electrocatalysis. Spectroscopic analysis reveals minimal intermediate species, indicative of rapid iodine redox kinetics with low energy barriers confirmed by theoretical calculations. Consequently, zinc-iodine batteries exhibit a remarkable lifespan of over 50 000 cycles with a capacity retention of 95.2%. This phase-junction engineering ensures the synergistic effect that accelerates charge migration and electrocatalysis, offering valuable insights to design advanced catalysts for zinc-iodine batteries and beyond.

1. Introduction

Zinc-iodine batteries have garnered significant attention due to their advantageous features, including the abundant availability of iodine (55 μg L^{-1} in seawater), a high discharge plateau (1.3 V vs Zn/Zn^{2+}), and a theoretical capacity (211 mAh g^{-1}).[1,2] Unlike traditional metal oxide cathodes (e.g., MnO_2, V_2O_5), which rely on intercalation reactions,[3,4] Zinc-iodine batteries operate on a solid–liquid conversion mechanism.[5] This approach circumvents the common structural collapse associated with the intercalation paradigm, providing a more stable framework for energy storage. However, several critical challenges need to be addressed to fully harness the potential of zinc-iodine batteries. One major obstacle is the inherently low electrical conductivity of iodine, which impedes efficient electron transfer during the redox conversion processes.[6] This limitation results in sluggish reaction kinetics, leading to reduced power output and lower overall battery efficiency. Additionally, the formation of highly soluble polyiodide species during redox reactions exacerbates the problem by causing a suboptimal utilization of iodine.[7] These soluble intermediates can migrate away from the electrode, leading to capacity decay, low Coulombic efficiency, and diminished battery lifespan.[8]

To overcome these challenges, the development of iodine-capturing substrates with high electrical conductivity, large specific surface areas, and robust catalytic activity for iodine redox reactions is essential. Recent research has focused on optimizing cathode materials by integrating porous carbon nanostructures,[9,10] tunnel-shaped Prussian blue analogs,[11] and layered MXenes.[12–15] These materials have shown promise in enhancing the performance of zinc-iodine batteries by providing a conducive environment for iodine retention and facilitating efficient redox reactions. Molybdenum carbide (Mo_xC) has emerged as a particularly promising material due to its high electronic conductivity, exceptional stability, and superior catalytic activity, which have been extensively leveraged in electrocatalysis for hydrogen evolution and oxygen reduction reactions.[16,17] The introduction of Mo_xC-based heterostructures, particularly those with phase junctions, holds great potential in promoting the rapid electron migration necessary for efficient iodine redox conversion.[18] The formation of a built-in electric field within these heterostructures would further accelerate the stepwise conversion of iodine species, enhancing the overall battery performance.[19] Especially, controlling the dispersion and phase formation of Mo_xC on nitrogen-doped carbon (NC) substrates is highly promising to optimize the electrochemical performance.[20] However, achieving the desired heterostructure features of Mo_xC through conventional thermal treatment methods poses significant challenges.[21] To the best of our knowledge, there has been no report on applying molybdenum carbide heterostructures to iodine redox catalysis or as cathode materials for zinc-iodine batteries.

S. Chen, J. Ma, Q. Chen, W. Shang, J. Liu, J. Shang, Y. Wang, J. Zhang
Key Laboratory for Colloid and Interface Chemistry
Ministry of Education
School of Chemistry and Chemical Engineering
Shandong University
Jinan 250100, China
E-mail: jtzhang@sdu.edu.cn

The ORCID identification number(s) for the author(s) of this article can be found under https://doi.org/10.1002/adfm.202505201

DOI: 10.1002/adfm.202505201

 © 2025 Wiley-VCH GmbH

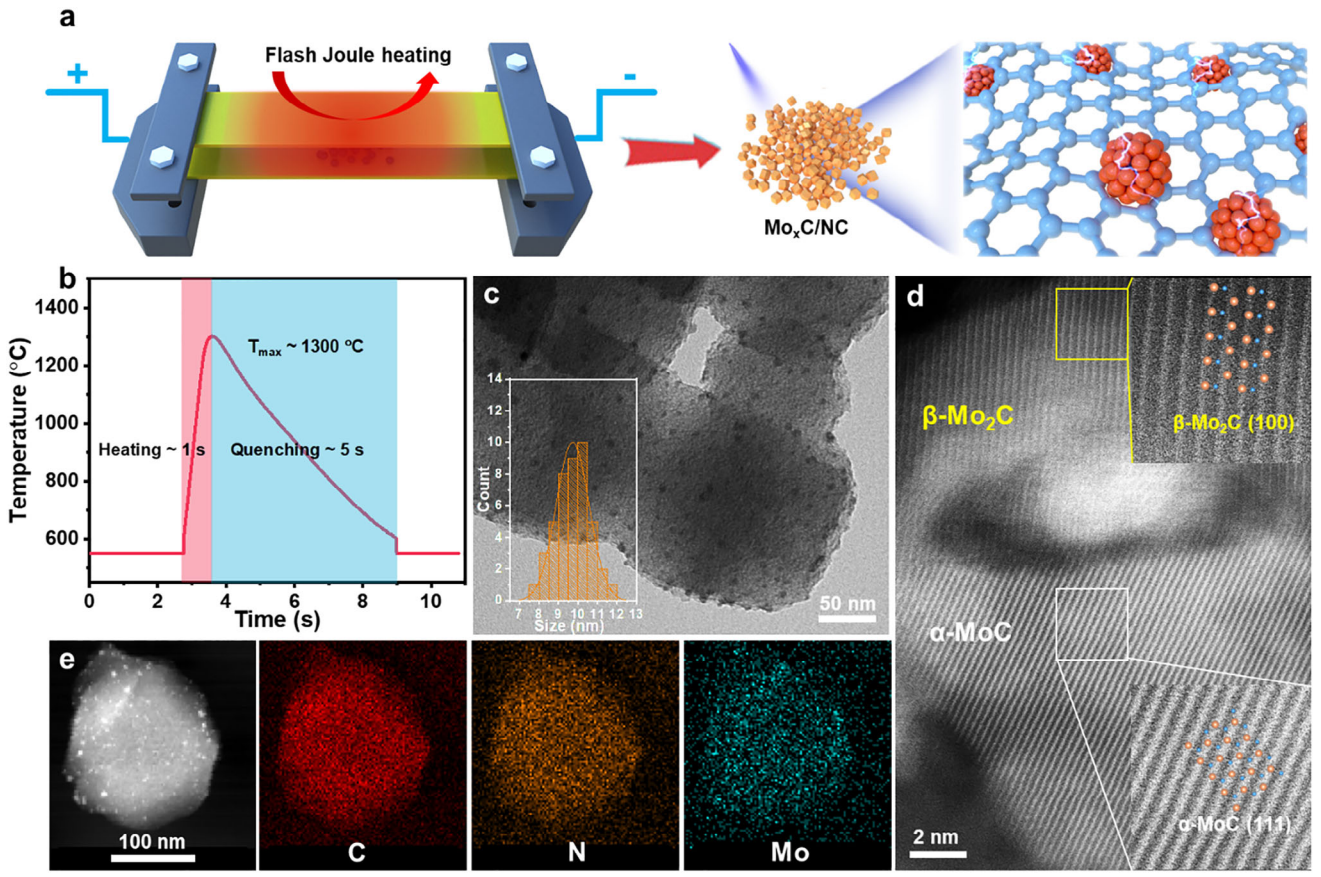

Figure 1. Synthesis and structure characterization of Mo_xC/NC. a) Schematic illustration for the synthesis of Mo_xC/NC by FJH method. b) Temperature-time curves during FJH treatment. c) TEM image, the insect is the statistical particle size distribution of α, β-Mo_xC/NC. d) HAADF-HRTEM image and the interface between α-MoC (111) and β-Mo_2C (100). e) EDS mapping images of C, N, and Mo elements.

Herein, uniform dispersion of small Mo_xC nanoparticles on NC was achieved through the thermal shock treatment, using ZIF-8 and $MoCl_5$ as carbon and molybdenum sources, respectively. The regulation of the atomic ratio in Mo_xC is feasible for the controllable synthesis of heterostructures via the flash Joule heating (FJH) method by modulating the heating process. Notably, a phase junction from α-MoC to β-Mo_2C was established on the NC, expediting the electron transfer for facile redox conversion reactions. The microporous structure of NC not only provides ample physical space for iodine loading and expediting the shuttling of soluble polyiodides, but also ensures sustained exposure of active sites for electrocatalytic conversion. As expected, the assembled zinc-iodine batteries deliver a high specific capacity of 261.8 mAh g^{-1} at 1 C and maintain a large capacity of 216.7 mAh g^{-1} at 20 C. Additionally, the remarkable capacity retention rate of 95.2% is achieved after 50 000 cycles, underscoring the importance of a well-designed phase-junction in promoting sequential iodine conversion and directed migration under the influence of adsorption difference among distinct active regions. The investigation into phase-junctions spatially propelling the stepwise redox conversion of iodine is expected to guide the rational design of high-performance batteries.

2. Results and Discussion

2.1. Morphology and Structure Characterization

The rapid heating capability of FJH equipment allows for a swift increase in temperature within seconds upon the application of an electric current (**Figure 1**a,b; Figure S1, Supporting Information),[22,23] thereby substantially improving synthesis efficiency. Typically, Molybdenum chloride ($MoCl_5$) undergoes thermodynamic sublimation to form vapors, subsequently engaging in a heterogeneous reaction with the solid carbon at elevated temperatures.[24] This interfacial gas–solid reaction leads to the nucleation and growth of molybdenum carbide (Mo_xC), dispersing uniformly throughout the carbonaceous matrix. A series of molybdenum carbides encapsulated in nitrogen-doped carbon (Mo_xC-NC, Table S1, Supporting Information) were synthesized by changing the molar ratio of $MoCl_5$ to NC and adjusting the duration of Joule heating. Notably, no particle aggregation is observed on the smooth surface of Mo_xC-NC (Figure S2, Supporting Information). However, transmission electron microscopy (TEM) images reveal that the distinct particles with an average size of 9.7 nm uniformly dispersed within the NC matrix (Figure 1c), but particle size remained unchanged despite

© 2025 Wiley-VCH GmbH

16163028, 0, Downloaded from https://advanced.onlinelibrary.wiley.com/doi/10.1002/adfm.202505201 by Shanxi University, Wiley Online Library on [09/05/2025]. See the Terms and Conditions (https://onlinelibrary.wiley.com/terms-and-conditions) on Wiley Online Library for rules of use; OA articles are governed by the applicable Creative Commons License

16163028, 0, Downloaded from https://advanced.onlinelibrary.wiley.com/doi/10.1002/adfm.202505201 by Shanxi University, Wiley Online Library on [09/05/2025]. See the Terms and Conditions (https://onlinelibrary.wiley.com/terms-and-conditions) on Wiley Online Library for rules of use; OA articles are governed by the applicable Creative Commons License

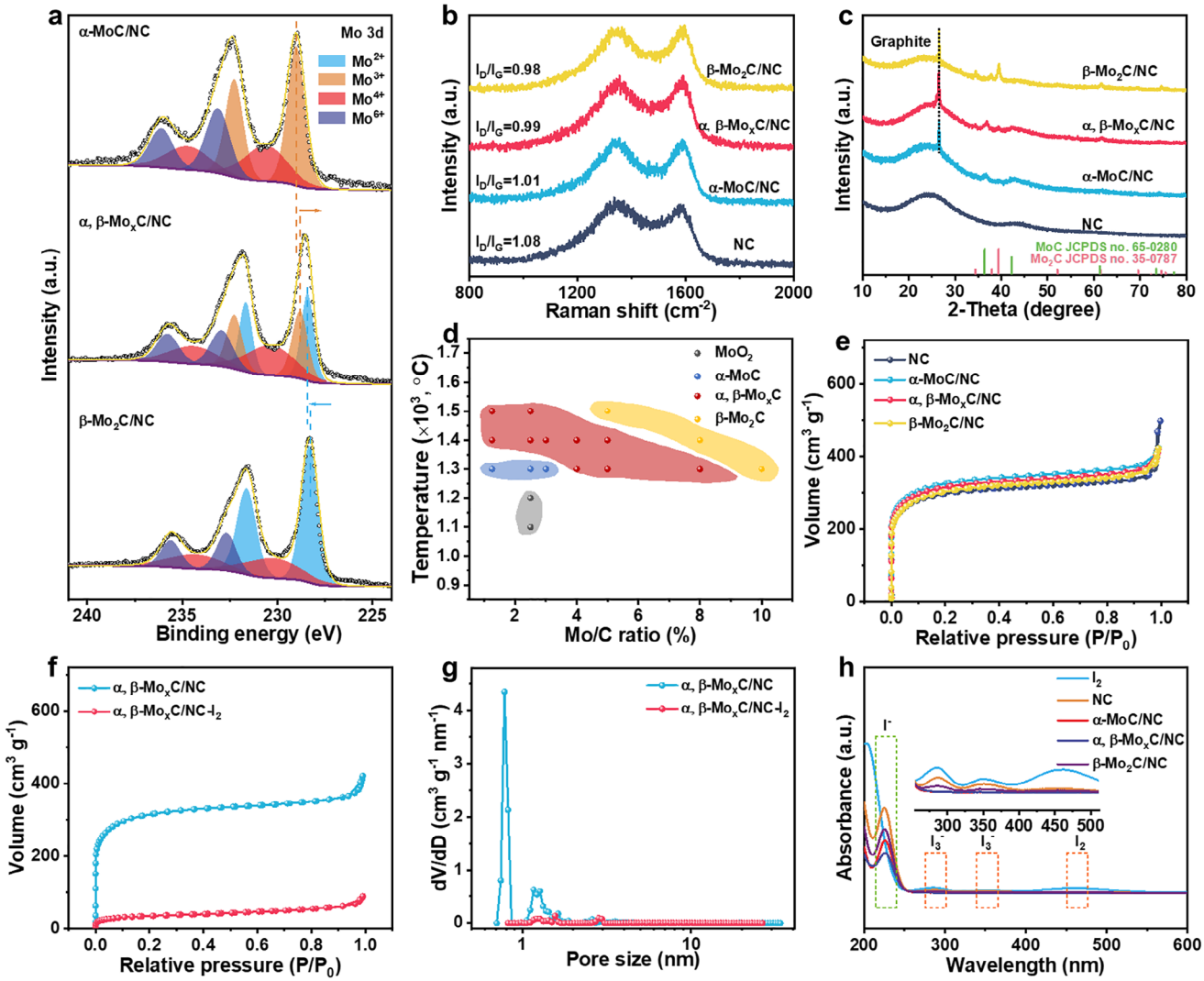

Figure 2. The spectra analysis of Mo_xC/NC. a) High-resolution XPS spectra of Mo 3d. b) Raman spectra and c) XRD patterns of NC, α-MoC/NC, α, β-Mo_xC/NC, and β-Mo_2C/NC. d) Plot showing the relationship between Mo_xC crystal forms with temperatures and Mo/C molar ratio. e) Nitrogen adsorption-desorption isotherms of NC, α-MoC/NC, α, β-Mo_xC/NC and β-Mo_2C/NC. f, g) Nitrogen adsorption-desorption isotherms and corresponding pore size distribution of α, β-Mo_xC/NC before and after iodine loading. h) UV–vis spectra of supernate after iodine adsorption test.

variations in the ratio of $MoCl_5$ (Figure S3, Supporting Information). High-angle annular dark-field scanning transmission electron microscopy (HAADF-STEM) image further elucidates the presence of distinct phase interfaces, with interplanar spacings of 0.246 and 0.261 nm corresponding to α-MoC (111) and β-Mo_2C (100), respectively (Figure 1d).[25] Element mapping images (Figure 1e) exhibit the homogeneous dispersion of C, N, and Mo within the molybdenum carbide phase-junction encapsulated in nitrogen-doped carbon (α, β-Mo_xC/NC).

X-ray photoelectron spectroscopy (XPS) analysis reveals that no residual Zn within the NC after calcination at 1000 °C (Figure S4a, Supporting Information), with the porous structure formed during the Zn evaporation process. The high-resolution C 1s spectrum of NC reveals four distinct deconvoluted peaks corresponding to C—C/C=C, C—O, C=O, and O—C=O functional groups (Figure S4b, Supporting Information), while an additional peak at 284.2 eV indicates the presence of C—Mo bonds in Mo_xC-NC.[26] The N 1s spectrum is resolved into four groups at 398.4, 399.6, 401, and 402.6 eV, corresponding to pyridinic-, pyrrolic-, graphitic-, and oxidized nitrogen species, respectively (Figure S4c, Supporting Information).[27] Notably, the proportion of graphitic nitrogen, identified as the most catalytically active nitrogen species for the iodine redox reaction,[28] increases with the $MoCl_5$ concentration. In the Mo 3d XPS spectrum (**Figure 2a**), two peaks at 228.4 and 231.6 eV are assigned to Mo^{2+} in β-Mo_2C/NC, while the peaks at 228.8 and 232.2 eV are attributed to Mo^{3+} in α-MoC/NC.[29] Specifically, the Mo^{2+} peak exhibits slight blueshifts (≈0.1 eV), and the Mo^{3+} peak a redshift (≈0.2 eV) in α, β-Mo_xC/NC, revealing the electron migration from β-Mo_2C to α-MoC at the phase junction.[21] Additionally, the appearance of Mo^{4+} and Mo^{6+} peaks would be attributed to the slight surface oxidation.[30] The FJH treatment notably increases the graphitization degree of NC, as evidenced by a reduced I_D/I_G ratio (Figure 2b), which in turn enhances the electronic

 © 2025 Wiley-VCH GmbH

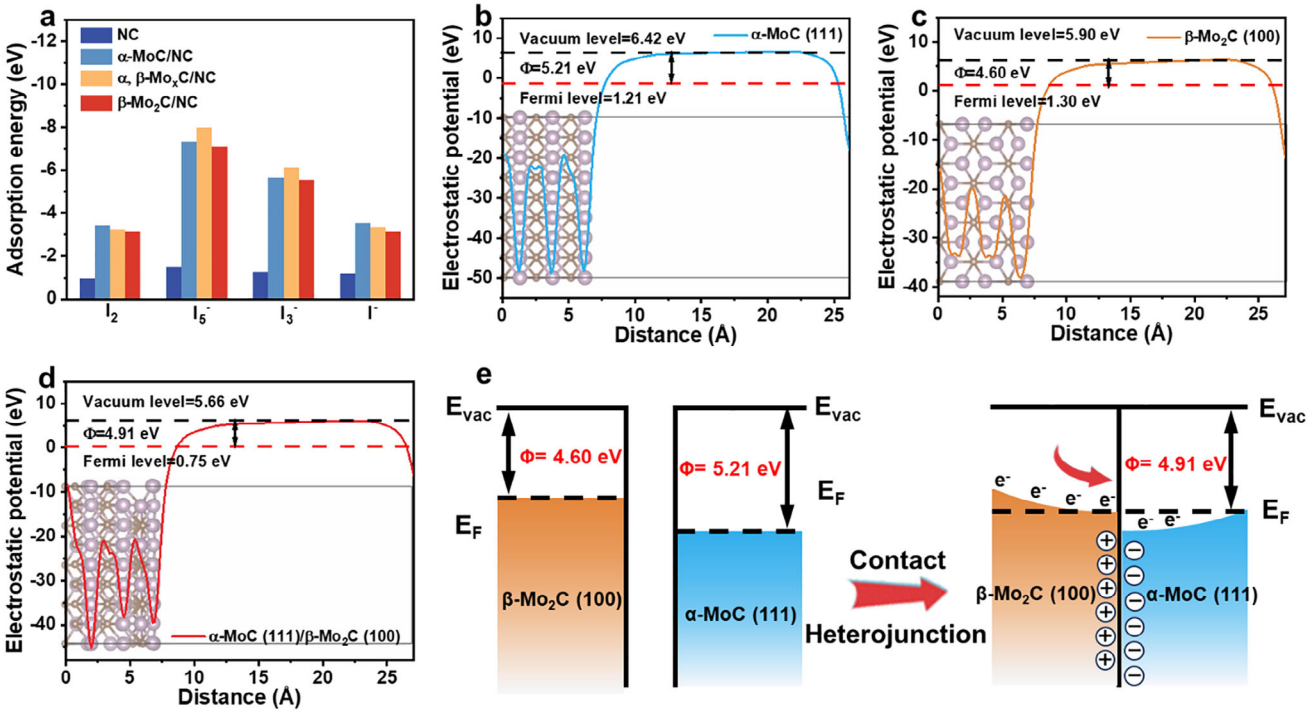

Figure 3. Theoretical calculation of heterostructures. a) DFT calculations of the adsorption energies between iodine species and various substrates. b–d) The electrostatic potentials of b) α-MoC (111), c) β-Mo_2C (100), and d) α-MoC (111)/β-Mo_2C (100) interface. e) Schematic illustration of energy level variations before and after contact.

conductivity to improve the rate performance. With increasing ratio of $MoCl_5$, a phase transformation from α-MoC to β-Mo_2C is observed (Figure 2c). Notably, MoO_2 is the prevalent phase below 1300 °C possibly due to the ambient air environment, whereas higher temperatures induce the formation of β-Mo_2C via a carbothermal reaction (Figure S5; Figure S6, Supporting Information). In comparison with the metastable nature of α-MoC,[31] the combination of elevated temperatures and increased $MoCl_5$ concentration enables the gradual formation of the thermodynamically stable β-Mo_2C (Figure 2d). Therefore, the phase junctions within Mo_xC-NC can be precisely controlled by adjusting the $MoCl_5$ ratio and thermal shock temperature, offering a versatile approach to tailoring the material properties for advanced electrocatalysis.

2.2. Iodine Species Adsorption Ability

The carbothermic reaction enables the formation of a highly porous structure (Figure S7, Supporting Information), thereby contributing to the increased specific surface area of α-MoC/NC (1065 $m^2\ g^{-1}$) and α, β-Mo_xC/NC (1019 $m^2\ g^{-1}$) in comparison with NC (934 $m^2\ g^{-1}$, Figure 2e; Table S2, Supporting Information). However, in the presence of excess $MoCl_5$, the specific surface area decreases, as observed with β-Mo_2C/NC (966 $m^2\ g^{-1}$). Upon successful encapsulation of iodine within the microporous framework, the specific surface area of α, β-Mo_xC/NC-I_2 decreases to 118 $m^2\ g^{-1}$, and the micropore structures vanish (Figure 2f,g). To evaluate the adsorption capacity in the iodine-saturated aqueous solution (Figure S8, Supporting Information), the rapid color fading compared to NC indicates enhanced adsorption ability due to the presence of Mo_xC particles. Ultraviolet-visible (UV–vis) spectroscopy (Figure 2h) exhibits the complete absence of I_2 and I_3^- peaks entirely after the adsorption test with α, β-Mo_xC/NC. The rapid decolorization and undetectable triiodides in $Zn(I_3)_2$ solution further unveil the robust adsorption capability of α, β-Mo_xC/NC for iodine species (Figures S9 and S10, Supporting Information).

To gain deeper insight into the enhanced adsorption capacity toward iodine species, Density functional theory (DFT) calculations (Figures S11–S14, Supporting Information) reveal the highest adsorption energy of the α-MoC (111) interface to I_2 and I^- (**Figure 3a**), and the preferential adsorption of the α-MoC (111)/β-Mo_2C (100) interface for polyiodides (I_5^-, I_3^-). The selective adsorption in distinct regions enables α, β-Mo_xC/NC to facilitate the stepwise conversion of iodine species.

2.3. Built-In Electric Field Analysis

The work functions of α-MoC (111) and β-Mo_2C (100) are calculated to be 5.21 and 4.6 eV, respectively (Figure 3b,c). This difference in energy levels drives spontaneous electron migration from β-Mo_2C (100) to α-MoC (111), leading to an equilibrium with a Fermi level of 0.75 eV at the contact interface (Figure 3d). Consequently, the accumulation of excess electrons at the α-MoC (111) site, and the generation of positive holes at β-Mo_2C (100) sites induces the formation of a built-in electric filed (Figure 3e). The charge density difference reveals the noticeable charge transfer from β-Mo_2C (100) to α-MoC (111) (Figure S15, Supporting

© 2025 Wiley-VCH GmbH

16163028, 0, Downloaded from https://advanced.onlinelibrary.wiley.com/doi/10.1002/adfm.202505201 by Shanxi University, Wiley Online Library on [09/05/2025]. See the Terms and Conditions (https://onlinelibrary.wiley.com/terms-and-conditions) on Wiley Online Library for rules of use; OA articles are governed by the applicable Creative Commons License

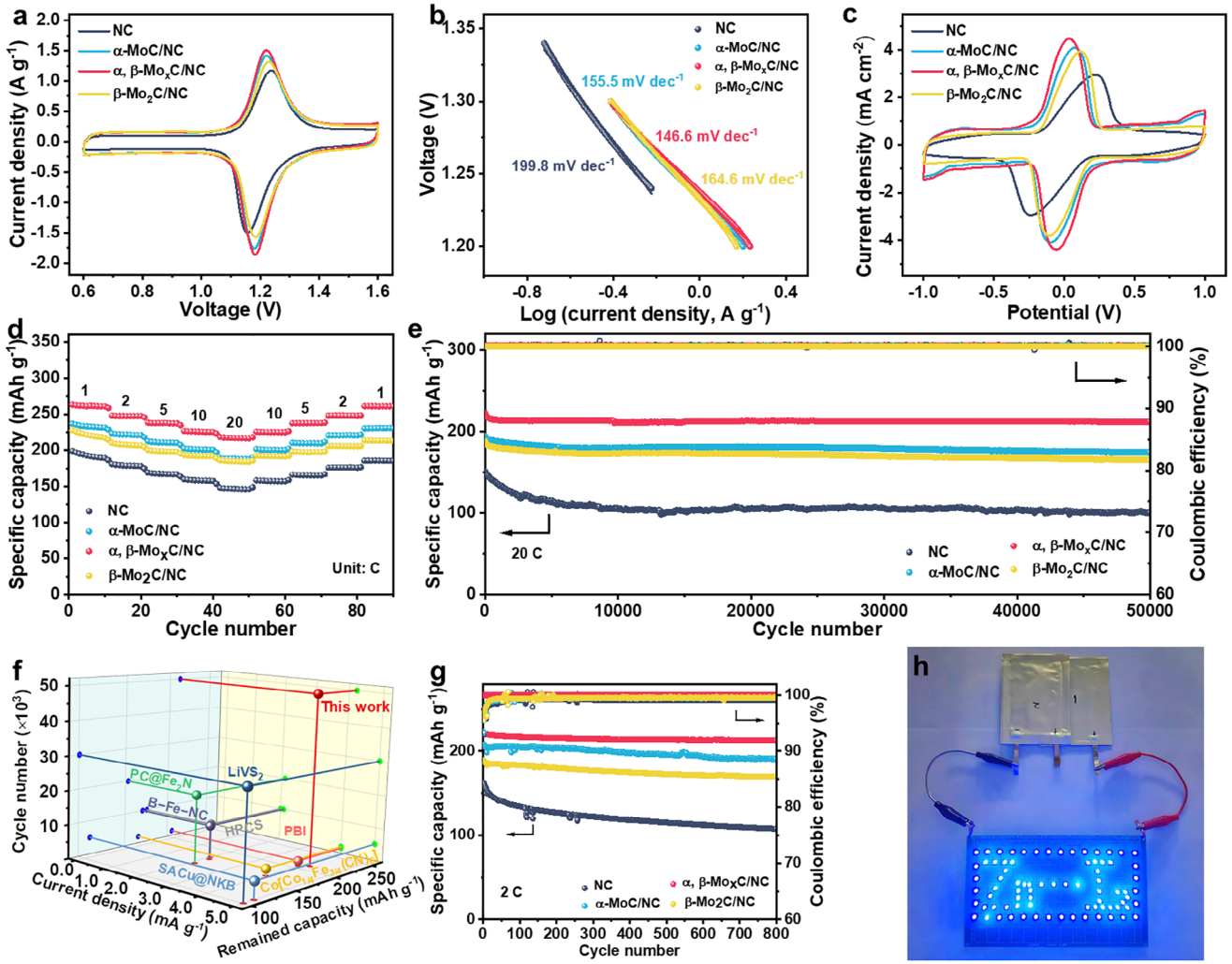

Figure 4. Electrochemical performance of the Zn-I_2 batteries. a) CV curves of the assembled Zn-I_2 batteries with NC, α-MoC/NC, α, β-Mo_xC/NC, and β-Mo_2C/NC cathodes. b) Tafel plots from the reduction peak of CV curves. c) CV curves of symmetric cells with different iodine hosts. d) Rate performance and e) long-term stability of Zn-I_2 batteries. f) Battery performance comparison with recent reports. g) Cycling stability of pouch cells at 2 C. h) Digital graph of two pouch cells with α, β-Mo_xC/NC cathode in series to light 78 LEDs.

Information), further confirming the formation of the built-in electric field. The charge redistribution at the phase junction would optimize the spatial distribution of active iodine species and enhance electron transfer, thus improving iodine conversion kinetics and alleviating the shuttle effect of polyiodides.

2.4. Electrochemical Performance of Zinc-Iodine Batteries

Zinc-iodine batteries were assembled to investigate the electrochemical performance with different catalytic hosts. As shown in **Figure** 4a, the symmetric redox peaks at around 1.2 V correspond to the iodine redox reaction. The voltage polarization (redox peaks gap) of NC, α-MoC/NC, α, β-Mo_xC/NC, and β-Mo_2C/NC are 82, 42, 37, and 44 mV, respectively, with the smallest polarization observed for α, β-Mo_xC/NC, suggesting the good redox reversibility. The Tafel slopes derived from the reduction peaks are 199.8, 155.5, 146.6, and 164.6 mV dec^{-1} for NC, α-MoC/NC, α, β-Mo_xC/NC, and β-Mo_2C/NC, respectively (Figure 4b), indicating favorable redox kinetics with α, β-Mo_xC phase-junctions. Symmetric cells were assembled to further assess catalytic activity (Figure 4c). The α, β-Mo_xC/NC delivers higher current response and lower voltage polarization than those of NC, α-MoC/NC and α, β-Mo_xC/NC, attributed to the built-in electric field at the phase-junction, which would accelerate the electrons transfer to ensure the fast iodine redox reactions. The batteries with α, β-Mo_xC/NC cathode exhibit larger specific capacities of 261.8, 247.2, 237.4, 225.6, and 216.7 mAh g^{-1} at 1, 2, 5, 10, and 20 C, respectively (Figure 4d), in comparison with NC, α-MoC/NC and β-Mo_2C/NC. The specific capacity exceeding the theoretical capacity is primarily attributed to the capacitive contribution of the porous carbon material (Figure S16, Supporting information). Long-term stability tests (Figure 4e) show a capacity retention of 95.2% after 50 000 cycles for the battery with the α, β-Mo_xC/NC cathode, superior to those with NC (66.5%), α-MoC/NC (89.8%), β-Mo_2C/NC (87.7%), and the results reported recently (Figure 4f).[9,11,32–36]

© 2025 Wiley-VCH GmbH

16163028, 0, Downloaded from https://advanced.onlinelibrary.wiley.com/doi/10.1002/adfm.202505201 by Shanxi University, Wiley Online Library on [09/05/2025]. See the Terms and Conditions (https://onlinelibrary.wiley.com/terms-and-conditions) on Wiley Online Library for rules of use; OA articles are governed by the applicable Creative Commons License

The morphology and crystalline structure of the Mo_xC particles are maintained after cycling, demonstrating the enhanced structure stability (Figure S17, Supporting information). The high structural stability and superior catalytic activity of α, β-Mo_xC/NC endow zinc-iodine batteries with excellent electrochemical performance at low current densities and under high loading conditions (60 wt%, Figure S18, Supporting information). Pouch cells with α, β-Mo_xC/NC cathode illustrate a high specific capacity of 213.1 mAh g^{-1} after 800 cycles, with a capacity retention of 95.9%, which is higher than the retention rates of 68.5, 91.5 and 89.6% observed for the NC, α-MoC/NC, and β-Mo_2C/NC cathodes, respectively (Figure 4g). Two pouch cells in series are able to illuminate 78 LEDs, demonstrating practical practicality (Figure 4h). Significantly, the assembled pouch cells exhibit an average capacity of 1.18 Ah stably with a loading of 15 mg cm^{-2}. Importantly, these cells show negligible capacity loss over 50 cycles ((Figure S19, Supporting information), further demonstrating the good stability and long-term effectiveness of the I_2 cathode under practical conditions. The enhanced anchoring effect of Mo_xC active sites to iodine species and the phase-junctions in α, β-Mo_xC/NC would accelerate the catalytic iodine conversion by enhancing the electron transfer, thus inhibiting the shuttling effect to improve the iodine utilization. Consequently, the batteries maintain high capacity retention after extensive cycling tests.

The self-discharge behaviors were evaluated using an intermittent galvanostatic charge/discharge test (Figure S20, Supporting Information). The zinc-iodine batteries with α, β-Mo_xC/NC cathode exhibit the highest capacity retention of 98.2%, surpassing those with NC (87.4%), α-MoC/NC (95.3%), and β-Mo_2C/NC (94.6%), manifesting the superior suppression of iodine dissolubility and the shuttling effect. Potentiostatic deposition experiments were conducted to investigate the nucleation and growth of I_2 on these substrates (Figure S21, Supporting Information). The α, β-Mo_xC/NC cathode exhibits the highest I_2 precipitation capacity of 134.5 mAh·g^{-1} on the basis of the iodide fraction in electrolyte, compared to NC (67.5 mAh·g^{-1}), α-MoC/NC (99.4 mAh·g^{-1}) and β-Mo_2C/NC (87.2 mAh·g^{-1}), demonstrating the facile nucleation kinetics of iodine on the α, β-Mo_xC/NC cathode.

2.5. Energy Storage Mechanism

To investigate the energy storage process, cyclic voltammetry (CV) analysis of the α, β-Mo_xC/NC cathode reveals negligible increases in redox peak separation with increasing scan rates, indicating excellent reversibility and low polarization (Figure S22, Supporting Information). The relationship between current (i) and scan rate (v) is expressed by the equation of $i = a^v b$.[37] The b-values deduced from the slope between log i and log v are 0.88 and 0.91 for oxidation and reduction peaks, respectively, unveiling the dominant capacitive behavior (Figure S23, Supporting Information). Further quantification using the equation of $i = k_1 v + k_2 v^{1/2}$ reveals capacitive contributions of 76.6, 79.1, 82.1, 85.8 and 91.9% at the scan rates of 0.2, 0.4, 0.6, 0.8 and 1 mV s^{-1}, respectively.[37] These values are higher than those of NC, α-MoC/NC, and β-Mo_2C/NC (Figures S24–S27, Supporting Information), attributing the enhanced capacitive behavior to the efficient electrocatalysis of heterostructures, which is inconsistent with the good rate performance of the batteries.

2.6. Catalytic Mechanism of Iodine Redox Conversion

In situ, Raman spectroscopy was utilized to monitor the redox conversion of iodine species during battery cycling. The presence of I_3^- and I_5^- species at 106 and 161 cm^{-1} are detected on the surface of the NC cathode, respectively owing to the charge transfer between the adsorbed I_2 and substrates (**Figure 5a**).[36] During the discharge process, these peaks gradually diminish, indicating a slow iodine conversion process. In contrast, for α, β-Mo_xC/NC cathode, the I_3^- and I_5^- peaks rapidly disappear at the discharge voltage of 1.2 V (Figure 5b), demonstrating faster and more efficient catalytic activity. The electron transfer number during the iodine reduction reaction (IRR) was calculated using the Koutecky-Levich equation (Figure S28, Supporting Information). The NC cathode exhibits an electron transfer number of 1.61, revealing the inadequate IRR due to poor catalytic activities. For comparison, the electron transfer number of α, β-Mo_xC/NC is calculated to be 1.96, suggesting a two-electron transfer process with the theoretical conversion from I_2 to I^-. This finding further demonstrates the excellent catalytic activity of α, β-Mo_xC/NC.

In situ, UV-vis spectroscopy tests further analyze the iodine conversion dynamics. Peaks corresponding to I_3^- species are observed at 286 and 350 nm.[38] During the charge process, the increase of peak intensities suggests the oxidation of I^- to I_3^- species. On the NC cathode, the increasing peak intensity reflects the dissolution of I_3^- into the aqueous electrolyte (Figure 5c) In contrast, for the α, β-Mo_xC/NC electrode, the lower peak intensities of I_3^- suggest minimized dissolution (Figure 5d), highlighting the electrode's superior adsorption and conversion properties.

Electrochemical impedance spectroscopy was performed to investigate the charge transfer kinetics during iodine redox. The α, β-Mo_xC/NC electrode exhibits a lower charge transfer resistance (R_{ct}) of 91.6 Ω, compared to NC (178.6 Ω), α-MoC/NC (116.7 Ω), and β-Mo_2C/NC (130.2 Ω, Figure S29a, Supporting Information). This suggests enhanced charge transfer due to the built-in electric field at the phase junctions. Significantly, the low Warburg factor further reveals the accelerated polyiodide diffusion rate, which stems from the preferential adsorption across the heterogeneous catalyst (Figure S29b, Supporting Information).[39] Subsequently, the activation energy (E_a) for the iodine conversion is determined according to the Arrhenius equation:

$$1/R_{ct} = A \exp\left(E_a/RT\right) \quad (1)$$

The calculated values for NC, α-MoC/NC, α, β-Mo_xC/NC, and β-Mo_2C/NC are 26.4, 19.0, 17.4, and 20.5 kJ mol^{-1}, respectively (Figure 5e–g; Figure S30 and Tables S3–S6, Supporting Information). The lowest activation energy of α, β-Mo_xC/NC manifests the outstanding catalytic activity toward the iodine redox reaction, leading to the rapid iodine conversion process observed.[39]

The Gibbs free energy changes (ΔG) analysis (**Figure 6a**) reveals that the conversion of I_2 to I^- is thermodynamically favorable, with the rate-determining step being the conversion of $^*I_3^-$ to $^*I^-$ due to the highest ΔG value. During charging, the oxidization of I^- to I_3^- on α, β-Mo_xC/NC has a ΔG value of 1.15 eV, lower than those of NC (2.35 eV), α-MoC/NC (1.50 eV) and β-Mo_2C/NC (2.12 eV), suggesting the energy-favorable iodine oxidation. Additionally, the lowest energy barrier for I_3^- dissociation (0.082 eV)

© 2025 Wiley-VCH GmbH

16163028, 0, Downloaded from https://advanced.onlinelibrary.wiley.com/doi/10.1002/adfm.202505201 by Shanxi University, Wiley Online Library on [09/05/2025]. See the Terms and Conditions (https://onlinelibrary.wiley.com/terms-and-conditions) on Wiley Online Library for rules of use; OA articles are governed by the applicable Creative Commons License

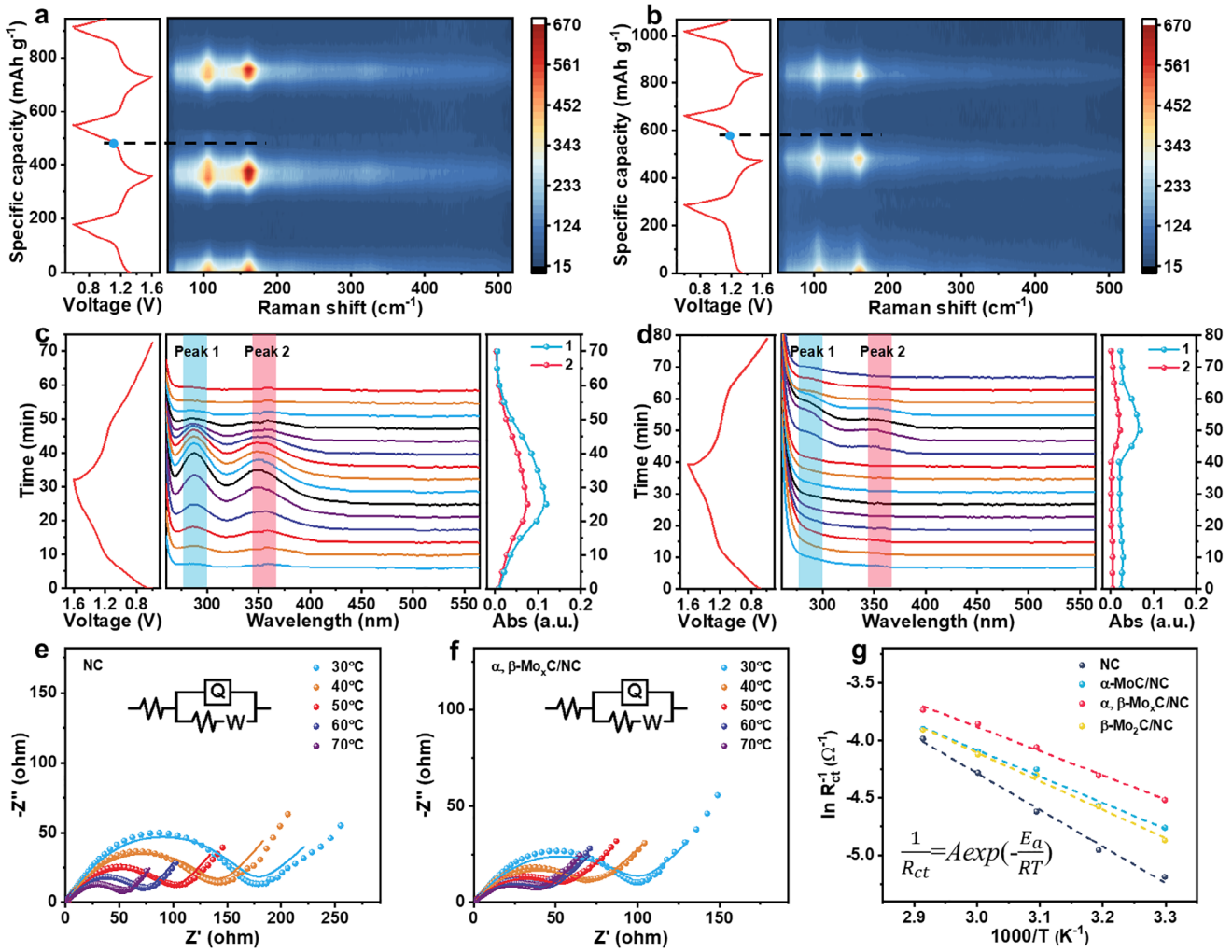

Figure 5. The analysis of the iodine conversion process. In-situ Raman and UV–vis spectra and corresponding voltage-time curves of Zn-I_2 batteries with a, c) NC and b, d) α, β-Mo_xC/NC cathodes. Nyquist plots of Zn-I_2 batteries with e) NC and f) α, β-Mo_xC/NC cathodes under different temperatures. g) Arrhenius curves and the activation energies are obtained from the slope of the fitted line.

on α, β-Mo_xC/NC further confirms the favorable reduction kinetics (Figure 6b; Figure S31, Supporting Information) to promote the rapid conversion of active iodine species and suppress the shuttle effect of polyiodides. The total density of states (TDOS) for α, β-Mo_xC/NC show increased electron density near the Fermi level (Figure 6c), indicating the enhanced conductive properties to contribute to the rapid electron migration.[40] The charge population analysis reveals substantial positive charge accumulation at the α-MoC (111)/β-Mo_2C (100) interface (Figure 6d; Figure S32, Supporting Information), reinforcing the strong chemisorption of polyiodides. Differential charge density plots reveal the preferable electron migration toward iodine species owing to the electronegativity difference (Figure 6e,f; Figures S33–S36, Supporting Information). Evidently, I_2 is prone to adsorb on the α-MoC/NC surface, with electron transferring to I_2 (0.385 e), while $I_5^-$and I_3^- are adsorbed on α, β-Mo_xC/NC with electron transfers of 1.358 and 1.206 e, respectively. The substantial charge transfer enhances the chemical interaction between host materials and iodine species, inducing the cleavage of internal chemical bonds within iodine species (Figure S37, Supporting Information).[41] As a result, the iodine conversion kinetics are significantly improved. On the basis of the experimental and theoretical calculation results (Figure 6g), the iodine redox mechanism proceeds through a stepwise process. Initially, I_2 is adsorbed on the surface of α-MoC, which exhibits the highest adsorption energy. As I_2 is reduced to I_5^- and I_3^- along with accepting electrons from the host. The generated polyiodides migrate to the α-MoC (111)/β-Mo_2C (100) phase junctions, where the stronger chemisorption occurs. Subsequently, further reduction to I^- occurs on the surface of β-Mo_2C. The built-in electric field and adsorption strength differences between the two phases enhance iodine species transfer and conversion efficiency. The encapsulated Mo_xC particles alter the surface polarity of hosts to enhance the chemisorption toward active iodine species, thus suppressing the shuttle effect and minimizing self-discharge. The phase-junctions formed between α-MoC and β-Mo_2C lower the energy barrier for iodine redox reactions, thus facilitating the reversible conversion of iodine in a thermodynamically and kinetically favorable way. More

© 2025 Wiley-VCH GmbH

16163028, 0, Downloaded from https://advanced.onlinelibrary.wiley.com/doi/10.1002/adfm.202505201 by Shanxi University, Wiley Online Library on [09/05/2025]. See the Terms and Conditions (https://onlinelibrary.wiley.com/terms-and-conditions) on Wiley Online Library for rules of use; OA articles are governed by the applicable Creative Commons License

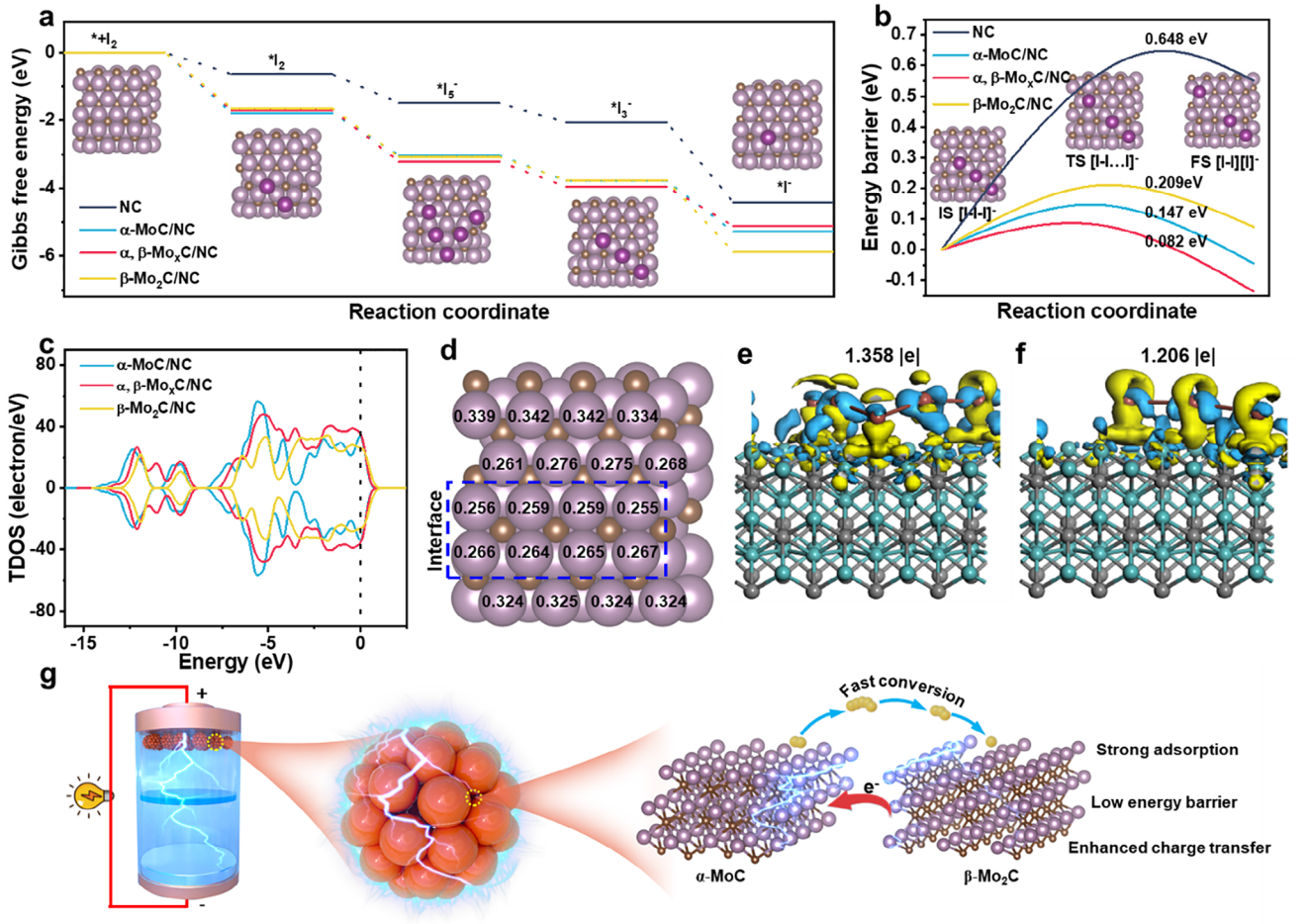

Figure 6. Theoretical calculation of the iodine redox mechanism. a) Gibbs free energy diagram of the I_2 reduction reaction on NC, α-MoC/NC, α, β-Mo_xC/NC and β-Mo_2C/NC. b) The dissociation energy barrier on various slabs. c) TDOS for different slabs. d) Mullikin charge distribution on α-MoC (111)/β-Mo_2C (100) interface. Charge density differences between e) I_5^-, f) I_3^- and α-MoC (111)/β-Mo_2C (100) interface, blue and yellow color represent charge accumulation and depletion, respectively. g) Schematic illustration of accelerating stepwise iodine conversion.

significantly, the built-in electric field within the phase junctions accelerates charge transfer, improving the conversion rate of active iodine intermediates. The preferable adsorption capabilities for active iodine species in distinct regions promote their stepwise transformation, thereby optimizing the utilization of active sites.

3. Conclusion

In summary, the Mo_xC nanoparticles, with favorable phase junctions were dispersed within the porous NC via the FJH method. The dual-phase structures of Mo_xC nanoparticles are adjustable by tuning the molar ratio of Mo to C and the heating temperature. The porous NC architecture effectively anchors iodine species, while the unique heterostructures of Mo_xC particles improve their chemisorption capability for iodine species. The advanced synthesis techniques enable the uniform dispersion of Mo_xC nanoparticles on NC, promoting the formation of phase junctions between α-MoC and β-Mo_2C. The α-MoC (111)/β-Mo_2C (100) phase-junction exhibits elevated catalytic activity toward the iodine conversion. DFT calculations confirm the phase junctions result in the lowest Gibbs free energy changes and reaction barriers for iodine redox reactions, endowing a thermodynamically and kinetically favorable way. Specifically, the built-in electric field established by the phase junction enhances charge transfer rates, thereby accelerating the transformation of active iodine species. Furthermore, the stepwise iodine transformation mechanism not only improves the efficiency of active site utilization, but also speeds up the iodine conversion process. The design strategy of employing phase-junction to accelerate stepwise iodine transformation offers new insights for designing advanced cathode materials for iodine batteries and beyond.

Supporting Information

Supporting Information is available from the Wiley Online Library or from the author.

Acknowledgements

This work was financially support by the financial support from the National Natural Science Foundation of China (22175108 & 22379086), the

 © 2025 Wiley-VCH GmbH

16163028, 0, Downloaded from https://advanced.onlinelibrary.wiley.com/doi/10.1002/adfm.202505201 by Shanxi University, Wiley Online Library on [09/05/2025]. See the Terms and Conditions (https://onlinelibrary.wiley.com/terms-and-conditions) on Wiley Online Library for rules of use; OA articles are governed by the applicable Creative Commons License

Natural Scientific Foundation of Shandong Province (ZR2022ZD27), and Taishan Scholars Program (No. tstp20221105). The authors also acknowledge the assistance of the Analytical Center for Structural Constituent and Physical Property of Core Facilities Sharing Platform, Shandong University, and the National Synchrotron Radiation Laboratory (NSRL) at the University of Science and Technology of China.

Conflict of Interest

The authors declare no conflict of interest.

Data Availability Statement

The data that support the findings of this study are available from the corresponding author upon reasonable request.

Keywords

built-in electric field, iodine conversion, molybdenum carbides, phase junction, zinc-iodine batteries

Received: February 28, 2025
Revised: March 20, 2025
Published online:

[1] G. Qu, H. Wei, S. Zhao, Y. Yang, X. Zhang, G. Chen, Z. Liu, H. Li, C. Han, *Adv. Mater.* **2024**, *36*, 2400370.
[2] W. Yan, Y. Liu, J. Qiu, F. Tan, J. Liang, X. Cai, C. Dai, J. Zhao, Z. Lin, *Nat. Commun.* **2024**, *15*, 9702.
[3] D. Kundu, B. D. Adams, V. Duffort, S. H. Vajargah, L. F. Nazar, *Nat. Energy* **2016**, *1*, 16119.
[4] Y. Yuan, R. Sharpe, K. He, C. Li, M. T. Saray, T. Liu, W. Yao, M. Cheng, H. Jin, S. Wang, *Nat. Sustain.* **2022**, *5*, 890.
[5] Y. Yang, S. Liang, J. Zhou, *Curr. Opin. Electrochem.* **2021**, *30*, 100761.
[6] J. Sun, H. Ma, D. Wang, *J. Alloys Compd.* **2023**, *947*, 169696.
[7] J. Ma, M. Liu, Y. He, J. Zhang, *Angew. Chem., Int. Ed.* **2021**, *60*, 12636.
[8] L. Zhang, J. Huang, H. Guo, L. Ge, Z. Tian, M. Zhang, J. Wang, G. He, T. Liu, J. Hofkens, *Adv. Energy Mater.* **2023**, *13*, 2203790.
[9] Q. Chen, S. Chen, J. Ma, S. Ding, J. Zhang, *Nano Energy* **2023**, *117*, 108897.
[10] B. Wulan, X. Cao, D. Tan, X. Shu, J. Ma, S. Hou, J. Zhang, *CCS Chem.* **2023**, *5*, 2415.
[11] L. Ma, Y. Ying, S. Chen, Z. Huang, X. Li, H. Huang, C. Zhi, *Angew. Chem., Int. Ed.* **2020**, *60*, 3791.
[12] X. Li, N. Li, Z. Huang, Z. Chen, G. Liang, Q. Yang, M. Li, Y. Zhao, L. Ma, B. Dong, Q. Huang, J. Fan, C. Zhi, *Adv. Mater.* **2021**, *33*, 2006897.
[13] M. Li, X. Wang, F. Li, L. Zheng, J. Xu, J. Yu, *Adv. Mater.* **2020**, *32*, 1907098.
[14] D. Cai, J. Yang, T. Liu, S.-X. Zhao, G. Cao, *Nano Energy* **2021**, *89*, 106452.
[15] S. Pei, J. Shao, D. Wang, Z. Zhou, Z. Zhang, C. Mao, J. Liu, Z. Li, G. Li, *J. Mater. Chem. A.* **2023**, *11*, 3682.
[16] X. Lu, L. Yu, J. Zhang, X. W. Lou, *Adv. Mater.* **2019**, *31*, 1900699.
[17] Z. Kou, W. Zang, Y. Ma, Z. Pan, S. Mu, X. Gao, B. Tang, M. Xiong, X. Zhao, A. K. Cheetham, L. Zheng, J. Wang, *Nano Energy* **2020**, *67*, 104288.
[18] Y. Li, J. Zhang, Q. Chen, X. Xia, M. Chen, *Adv. Mater.* **2021**, *33*, 2100855.
[19] H. Li, C. Chen, Y. Yan, T. Yan, C. Cheng, D. Sun, L. Zhang, *Adv. Mater.* **2021**, *33*, 2105067.
[20] M. Zhao, P. Tan, D. Cai, Y. Liu, C. Zhang, B. Fei, B. Sa, Q. Chen, H. Zhan, *Adv. Funct. Mater.* **2023**, *33*, 2211505.
[21] X. Du, R. Zhang, D. Li, C. Hu, H. Garcia, *J. Energy Chem.* **2022**, *73*, 68.
[22] Y. Han, M. Liu, L. Sun, S. Li, G. Li, W. Song, Y. Wang, Z. Nan, S. Ding, H. Liao, Y. Yao, G. D. Stucky, F. R. Fan, Z. Tian, *Proc. Natl. Acad. Sci. U.S.A.* **2022**, *119*, 2121848119.
[23] A. Zhou, W. Guo, Y. Wang, J. Zhang, *J.Electrochem* **2022**, *28*, 2214007.
[24] J. Lu, H. Hugosson, O. Eriksson, L. Nordström, U. Jansson, *Thin Solid Films* **2000**, *370*, 203.
[25] C. Li, Z. Wang, M. Liu, E. Wang, B. Wang, L. Xu, K. Jiang, S. Fan, Y. Sun, J. Li, K. Liu, *Nat. Commun.* **2022**, *13*, 3338.
[26] P. Yin, H. Cai, X. Zhang, B. Chen, Y. Liu, R. Gao, C. Shi, *New J. Chem.* **2021**, *45*, 10396.
[27] L. Li, C. Tang, Y. Zheng, B. Xia, X. Zhou, H. Xu, S.-Z. Qiao, *Adv. Energy Mater.* **2020**, *10*, 2000789.
[28] T. Liu, H. Wang, C. Lei, Y. Mao, H. Wang, X. He, X. Liang, *Energy Storage Mater.* **2022**, *53*, 544.
[29] W. Liu, X. Wang, F. Wang, K. Du, Z. Zhang, Y. Guo, H. Yin, D. Wang, *Nat. Commun.* **2021**, *12*, 6776.
[30] K. Murugappan, E. M. Anderson, D. Teschner, T. E. Jones, K. Skorupska, Y. Román-Leshkov, *Nat. Catal.* **2018**, *1*, 960.
[31] B. Deng, Z. Wang, W. Chen, J. T. Li, D. X. Luong, R. A. Carter, G. Gao, B. I. Yakobson, Y. Zhao, J. M. Tour, *Nat. Commun.* **2022**, *13*, 262.
[32] M. Liu, Q. Chen, X. Cao, D. Tan, J. Ma, J. Zhang, *J. Am. Chem. Soc.* **2022**, *144*, 21683.
[33] W. Gao, S. Cheng, Y. Zhang, E. Xie, J. Fu, *Adv. Funct. Mater.* **2023**, *33*, 2211979.
[34] F. Yang, J. Long, J. A. Yuwono, H. Fei, Y. Fan, P. Li, J. Zou, J. Hao, S. Liu, G. Liang, Y. Lyu, X. Zheng, S. Zhao, K. Davey, Z. Guo, *Energy Environ. Sci.* **2023**, *16*, 4630.
[35] Y. Du, R. Kang, H. Jin, W. Zhou, W. Zhang, H. Wang, J. Qin, J. Wan, G. Chen, J. Zhang, *Adv. Funct. Mater.* **2023**, *33*, 2304811.
[36] P. F. Zhang, J. H. Li, S. J. Zhang, D. C. Li, S. Y. Zeng, S. L. Xu, Q. X. Yao, L. Y. Liu, L. Ding, H. X. Li, Y. Y. Hu, J. T. Li, Y. Zhou, *Adv. Funct. Mater.* **2023**, *34*, 2306359.
[37] Q. He, T. Hu, Q. Wu, C. Wang, X. Han, Z. Chen, Y. Zhu, J. Chen, Y. Zhang, L. Shi, X. Wang, Y. Ma, J. Zhao, *Adv. Mater.* **2024**, *36*, 2400888.
[38] Y. Lyu, J. A. Yuwono, P. Wang, Y. Wang, F. Yang, S. Liu, S. Zhang, B. Wang, K. Davey, J. Mao, Z. Guo, *Angew. Chem., Int. Ed.* **2023**, *62*, 202303011.
[39] X. Wu, Y. Guo, J. Su, J. Xiong, Y. Zhang, L. Wan, *Adv. Energy Mater.* **2013**, *3*, 1155.
[40] M. Gu, C. Lai, I. Ni, C. Wu, C. Chen, *Angew. Chem., Int. Ed.* **2023**, *62*, 202214963.
[41] P. Hei, Y. Sai, W. Li, J. Meng, Y. Lin, X. Sun, J. Wang, Y. Song, X. Liu, *Angew. Chem., Int. Ed.* **2024**, *63*, 202410848.

 © 2025 Wiley-VCH GmbH

16163028, 0, Downloaded from https://advanced.onlinelibrary.wiley.com/doi/10.1002/adfm.202505201 by Shanxi University, Wiley Online Library on [09/05/2025]. See the Terms and Conditions (https://onlinelibrary.wiley.com/terms-and-conditions) on Wiley Online Library for rules of use; OA articles are governed by the applicable Creative Commons License